JCB Journal of Cell Biology

TOOLS

Visualizing intra-Golgi localization and transport by side-averaging Golgi ministacks

Hieng Chiong Tie, Divyanshu Mahajan, and Lei Lu

The mammalian Golgi comprises tightly adjacent and flattened membrane sacs called cisternae. We still do not understand the molecular organization of the Golgi and intra-Golgi transport of cargos. One of the most significant challenges to studying the Golgi is resolving Golgi proteins at the cisternal level under light microscopy. We have developed a side-averaging approach to visualize the cisternal organization and intra-Golgi transport in nocodazole-induced Golgi ministacks. Side-view images of ministacks acquired from Airyscan microscopy are transformed and aligned before intensity normalization and averaging. From side-average images of >30 Golgi proteins, we uncovered the organization of the pre-Golgi, cis, medial, trans, and trans-Golgi network membrane with an unprecedented spatial resolution. We observed the progressive transition of a synchronized cargo wave from the cis to the trans-side of the Golgi. Our data support our previous finding, in which constitutive cargos exit at the trans-Golgi while the secretory targeting to the trans-Golgi network is signal dependent.

Introduction

In eukaryotes, proteins or lipids (cargos) synthesized in the ER are exported via the ER exit site (ERES) to the ER and Golgi intermediate compartment (ERGIC). Next, cargos transit the Golgi complex before being sorted to various post-Golgi destinations such as the plasma membrane (PM) or the endolysosome. The mammalian Golgi complex comprises laterally connected Golgi stacks. Each Golgi stack has four to seven flattened and tightly packed membrane sacs termed cisternae. A Golgi stack spans 200–400 nm from the cis to the trans side, which is in the range of the spatial resolution of a conventional light microscope (~250 nm). Although conventional and especially superresolution light microscopy can resolve the intra-Golgi localization to various extents, the results are mainly qualitative and reveal only the relative cisternal distributions of two to three proteins in individual Golgi stacks (Bottanelli et al., 2016; Dejgaard et al., 2007; Hao et al., 2021; Tie et al., 2016; Zhang et al., 2020). In contrast, complete understanding of the molecular and cellular organization of the Golgi demands quantitative and systematic imaging methods to localize the Golgi proteome, which comprises ~1,000 proteins (Chen et al., 2010).

Dejgaard et al. (2007) previously proposed quantitatively localizing a Golgi protein by intensity linescan or peak distances for nocodazole-induced Golgi ministacks (hereafter referred to as ministacks). We have recently developed a numerical method called Golgi localization by imaging the center of mass (GLIM) to reveal the sub-Golgi localization at a nanometer resolution (Tie et al., 2017; Tie et al., 2016). In this method, we similarly used nocodazole to disperse the densely congregated Golgi stacks into dozens of well-separated ministacks. Extensive studies have demonstrated that unlike acute treatment (Fourriere et al., 2016), ministacks under prolonged nocodazole treatment (≥3 h, the condition GLIM uses) are valid representations of the native Golgi stack (Cole et al., 1996; Rogalski et al., 1984; Tie et al., 2018; Trucco et al., 2004; Van De Moortele et al., 1993), although the intra-Golgi transport of large secretory cargos might be compromised in ministacks (Lavieu et al., 2014). In GLIM, coordinates of Golgi proteins are acquired with nanometer accuracy by their centers of fluorescence mass. The relative positions of Golgi proteins along the cis–trans axis are subsequently calculated as the localization quotient, *LQ* (Tie et al., 2016). We have generated a molecular map of the Golgi comprising *LQ*s of several dozen proteins and successfully monitored the intra-Golgi trafficking of secretory cargos (Tie et al., 2018; Tie et al., 2016). However, GLIM provides only a numerical value, *LQ*, instead of a visual image. Furthermore, *LQ* indicates the center of the fluorescence mass of a Golgi protein but not its axial distribution within the ministack. Thus, for example, a Golgi protein that evenly distributes from the cis- to the trans-Golgi can have the same *LQ* value as the one that exclusively localizes to the medial-Golgi region.

Following our en face averaging method to study the lateral distribution of Golgi proteins (Tie et al., 2018), we developed a

School of Biological Sciences, Nanyang Technological University, Singapore, Singapore.

Correspondence to Lei Lu: lulei@ntu.edu.sg.

side-averaging method to visualize the axial distribution of a Golgi protein directly. Using this novel tool, we resolved the cisternal organization of the ministack along its axis. In addition, we observed the progressive transport of secretory cargos from the cis to the trans side of a ministack.

Results

The axial size of a ministack is conserved

Under Airyscan microscopy, ministacks appear as randomly oriented disks (Tie et al., 2018). A ministack's side and en face view can be identified by the rim-localized Golgi proteins, such as giantin, GPP130, and golgin-84, which display as a pair of closely adjacent puncta (double-punctum) and a ring in the side and en face view, respectively (Tie et al., 2018; Fig. S1 A). Previously, we demonstrated that the N-termini of golgins such as giantin, GCC185, and GM130 are closely adjacent to their C-terminal membrane anchors (Tie et al., 2018). Therefore, the giantin-ring stained by anti-N-terminus antibody should closely represent the membrane at the cisternal rim. Fourriere et al. (2016) reported that, under acute nocodazole treatment, newly assembled ministacks initially lack certain Golgi proteins such as giantin, which are gradually acquired by ministacks after extended treatment. Under our nocodazole treatment (≥3 h), we found that almost all ministacks were positive for giantin (Fig. S1 A), suggesting that ministacks might be homogeneous in the organization and functionally matured.

To gain further understanding of the molecular organization of the Golgi, we conducted a morphometric analysis of ministacks using their side-views. Table S1 lists all morphometric variables used or defined in this study. To measure the ministack's lateral size, we adopted the distance between the two giantin puncta, the largest among known Golgi markers (Tie et al., 2018). We fitted the line intensity profile across the giantin double-punctum (Fig. S1 B), orthogonal to the Golgi axis, to the two-peak Gaussian function. The lateral size of giantin is defined as the distance between the two outer half maxima (Fig. S1 B). Similarly, the lateral line intensity profile of GM130, which localizes to the interior of the cis-cisternae (Tie et al., 2018), was fitted to a super-Gaussian function (Fig. S1 C). The lateral size of GM130 was calculated as the full width at half maximum (FWHM). We found that the axial line intensity profile of a Golgi protein follows the Gaussian distribution. The Gaussian center was used to indicate the axial position of the protein (Fig. S1, B and C). Therefore, the axial distance between two proteins is defined as the distance between their Gaussian centers. Since GM130 and GalT-mCherry localize to the cis and the trans regions of a ministack, the axial distance between them is defined as the axial size of the ministack (Table S1). Our morphometric data revealed that, while the lateral size of giantin varied from 400 to 1,200 nm, the axial size of the ministack was distributed at 274 ± 5 nm (mean ± SEM; n = 204; Fig. 1 A), suggesting that the axial size of a ministack is likely independent of its lateral size and remains roughly constant. A similar observation was also made for the axial distance from GM130 to giantin (Fig. 1 B).

In contrast to the conserved axial size of a ministack, the lateral size of GM130 as well as the lateral width of giantin puncta, which is the mean of the two FWHMs of puncta, were observed to change in proportion to the lateral size of giantin (Fig. 1, C and D), suggesting that the lateral organization of a ministack might vary proportionally. Previously, we showed that axial distances of Golgi proteins maintain the same ratios in ministacks, as demonstrated by their *LQ*s (Tie et al., 2016). Here, our observations revealed an additional morphological feature of the Golgi ministack, i.e., the axial size is conserved while the lateral size varies in proportion (Fig. 1 E). The finding is the basis for our side-averaging method described below.

Development of the side-averaging method

We hypothesized that ministack side-views could be aligned, normalized, and averaged to extract intrinsic structural features. To that end, we developed the below protocol as illustrated in Fig. 1 F (Materials and methods), taking advantage of our above morphometric findings. Ministacks are labeled for the protein of interest together with giantin to facilitate the identification of side-views. Subsequently, the side-view image is cropped, background-subtracted, and subjected to the following transformation steps. (1) The ministack is first translated so that the center of the fluorescence mass (hereafter referred to as fluorescence center) of giantin double-punctum coincides with the image center. (2) The image is then rotated to ensure that the two centers of puncta are parallel to the x axis. (3) Following that, the image is laterally expanded along the x axis so that centers of puncta are 80 pixels from the image center. (4) Next, the image is axially expanded along the y axis by eightfold. (5) The image canvas is subsequently adjusted to a square of fixed dimension (701 × 701 pixel), and the total intensity of each channel is normalized to 5×10^7. The intensity normalization is necessary so that each image has the same weightage in subsequent averaging. (6) Finally, the resulting images of the protein of interest are averaged. The side-average image is further linearly re-scaled along the x and y axis (Materials and methods) so that (1) the axial distance between GM130 and GalT-mCherry is 274 nm and (2) the lateral size of giantin is 700 nm (Fig. 1 A). Therefore, our side-average image is isotropic in scale and represents a typical ministack. We have developed Fiji macros (Data S1 and Data S2) to perform these procedures semiautomatically.

As an example, Fig. 1 G shows the processing of raw side-view images of giantin. Although individual side-views appeared diverse morphologies, averaging these images according to steps 1–6 resulted in a convergent side-view image characteristic of the distribution of giantin. One of the factors limiting us from getting higher-quality side-average images is the small sample size. It is hard to find side-views of ministacks, and we found that the number of analyzable side-views is usually less than one-third that of en face views. A large sample size is generally desirable to yield a smoother and more reflection-symmetrical side-average image. Therefore, we selected n = 16 as the cutoff for this study.

The cisternal distribution of Golgi proteins from side-averaging

We applied the side-averaging method to 38 Golgi proteins, 9 endogenous and 29 fluorescence protein or Myc-tagged ones.

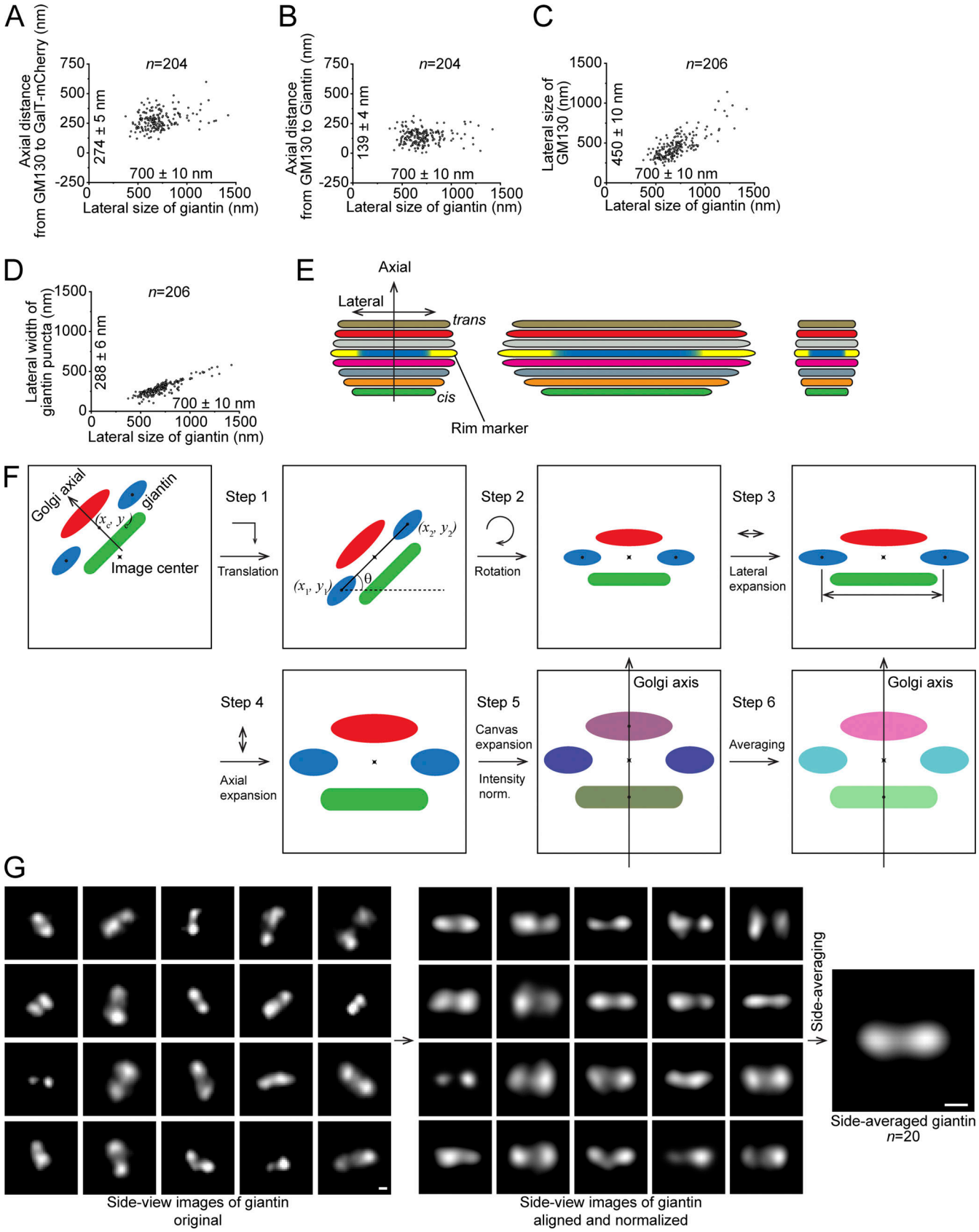

Figure 1. **The morphometric analysis and side-averaging of Golgi ministacks. (A–D)** The axial size of the ministack is approximately conserved, while lateral sizes of ministack cisternae vary in direct proportion. HeLa cells expressing GalT-mCherry were nocodazole-treated and immunostained for GM130 and giantin. Ministacks were subsequently imaged and subjected to morphometric analysis. In A and B, the axial distance from GM130 to GalT-mCherry (which is

also the axial size of the ministack; A) or giantin (B) against the lateral size of giantin is plotted. In C and D, the lateral size of GM130 (C) or lateral width of giantin punctum (D) against the lateral size of giantin is plotted. Numbers adjacent to the x and y axis are mean ± SEM values of variables corresponding to the x and y axis, respectively. *n*, the number of ministacks analyzed. **(E)** Schematic diagram illustrating the morphometric changes of Golgi ministacks: the axial sizes are conserved while the lateral ones vary proportionally. The two yellow segments schematically represent the distribution of a rim marker. **(F)** Schematic diagram showing the method of side-averaging. The two blue ovals represent the giantin double-punctum. (x_c, y_c) is the fluorescence center of giantin. (x_1, y_1) and (x_2, y_2) are fluorescence centers of the left and right giantin punctum, respectively. Intensity norm., intensity normalization. **(G)** An example of side-averaging. HeLa cells were processed as in F. 20 side-view images of giantin were aligned and normalized, and the resulting side-averaged image is shown at the right. Scale bar, 200 nm.

As indicated by their *LQ*s (Tie et al., 2016), their steady-state localization ranged from the ERES/ERGIC ($LQ < -0.25$), cis ($-0.25 \le LQ < 0.25$), medial ($0.25 \le LQ < 0.75$), trans-Golgi ($0.75 \le LQ < 1.25$) to TGN ($1.25 \le LQ$). We selected 10 GFP-tagged Golgi proteins to assess the effect of overexpression on localization. We plotted the *LQ* against the corresponding relative expression level of a protein for each ministack (Fig. S1 D). The relative expression level was calculated as the ratio of the integrated intensity of the protein to that of endogenous GM130. Our plots demonstrated that overexpression seems not to grossly affect the *LQ*, a quantitative metric for the axial localization. However, we could not rule out the effect of overexpression on lateral localization.

Side-average images of these 38 Golgi proteins indicate the axial distribution (first row of Fig. 2, A–D and G; and Fig. S2, A–E), quantitatively presented by the axial line intensity profile (second row of Fig. 2, A–D and G; and Fig. S2, A–E). All Golgi proteins examined in this study display a single-peak or unimodal axial distribution, a conclusion that cannot be made by analyzing their en face views or *LQ*s. Furthermore, side-averaging resolved the cisternal or sub-Golgi localization of proteins along the Golgi axis. Here, we define the axial position of the Golgi protein *i* as the *y* component of its fluorescence center's coordinate, y_i. Therefore, according to GLIM, we can directly calculate the *LQ* of protein *i*, termed LQ^{side} to distinguish it from the *LQ* acquired using GLIM. Both *LQ* and LQ^{side} are metrics of the axial localization of a Golgi protein, but LQ^{side} is calculated from the side-average. Using GM130 and GalT-mCherry as references (Tie et al., 2016), LQ^{side} is calculated as below.

$$LQ^{side} = \frac{y_i - y_{GM130}}{y_{GalT-mCherry} - y_{GM130}}$$

As shown in Table 1, the LQ^{side} of a Golgi protein is similar to the corresponding *LQ*. However, the former is expected to be less accurate primarily due to the smaller sample size.

The lateral line intensity profile (third row of Fig. 2, A–D and G; and Fig. S2, A–E) quantitatively describes the lateral distribution. For typical cisternal rim-localized proteins, such as giantin, GPP130, ACBD3, and GOLPH3, two peaks are discernable, although less clear than the corresponding radial mean intensity profiles of en face average images (fourth and fifth rows of Fig. 2, A–D and G; and Fig. S2, A–E). The normalized lateral size of a Golgi protein, calculated by the lateral size of the Golgi protein divided by that of giantin, agrees with the normalized diameter obtained from the radial mean intensity profile. The observation that normalized lateral sizes of Golgi enzymes (indicated within parentheses), such as MGAT2 (0.55), ST6GAL1 (0.67), and GalT-mCherry (0.67), are smaller than those of the corresponding cisternal rim markers with similar *LQ*s, such as giantin (1.00), GPP130 (0.90), and GOLPH3 (0.87), is consistent with our previous observation on the interior localization of enzymes within cisternae (Tie et al., 2018). This notion can be further visualized in the composite side-average images (Fig. 2, E and F). Next, we estimated lateral sizes of cisternae using rim markers (Table 1). From the cis- to the trans-Golgi, the normalized lateral sizes of rim markers (indicated in parentheses), including ACBD3 (0.72), giantin (1.00), GPP130 (0.90), and GOLPH3 (0.87), increase and then decrease, peaking at giantin. Therefore, consistent with our composite side-average images (Fig. 2 F), our morphometric analysis demonstrated the spindle shape of the ministack, which was previously observed by our en face averaging (Tie et al., 2018) and noticeable in the EM tomography of plant Golgi ministacks (Staehelin and Kang, 2008).

TGN proteins have two types of morphologies in side-average (Figs. 2 G and S2 E). Some TGN proteins, such as golgin-97, Cab45, Vamp4, SMS1, and furin, appear as a compact lump along the Golgi axis (Fig. S2 E), similar to Golgi stack proteins (Fig. 2, B–D; and Fig. S2, B–D). However, other TGN proteins appear to have dramatically different side and en face averages from Golgi stack proteins (Figs. 2 G and S2 E), consistent with our previous report (Tie et al., 2018). For example, clathrin coat machinery and its transmembrane cargos, such as clathrin light chain B (CLCB), GGA2, γ-adaptin, and CI-M6PR, scatter away from the stacked region and compact lumps of golgin-97, Cab45, Vamp4, SMS1, and furin as puncta (Figs. 2 G and S2 E).

We compared our side-average data with corresponding published EM localization results in Table S2, which includes sec16a (Hughes et al., 2009), sec31a (Tang et al., 2000), GS27 (Hay et al., 1998), ERGIC53 (Klumperman et al., 1998), GM130 (Trucco et al., 2004), γ1COP (Moelleken et al., 2007), βCOP (Orci et al., 1997), MGAT2 (Tie et al., 2018), giantin (Koreishi et al., 2013; Trucco et al., 2004), GPP130 (Tie et al., 2018), GalT-mCherry (Trucco et al., 2004), Rab6 (Antony et al., 1992), GOLPH3 (Bell et al., 2001), GGA1 (Puertollano et al., 2003), CI-M6PR (Doray et al., 2002), Vamp4 (Steegmaier et al., 1999), furin (Bosshart et al., 1994), CLCB (Staehelin and Kang, 2008), GGA2 (Doray et al., 2002), and γ-adaptin (Doray et al., 2002). Our comparison demonstrates that side-averaging is generally consistent with EM in localizing proteins with sub-Golgi accuracy. Sec16a seems to be the only one with the gross discrepancy in Table S2. Our side-averaging localizes it to the cis-Golgi (LQ^{side} = 0.04; Fig. S2 A), which does not agree with its well-documented ERES localization (Bhattacharyya and Glick, 2007; Hughes et al.,

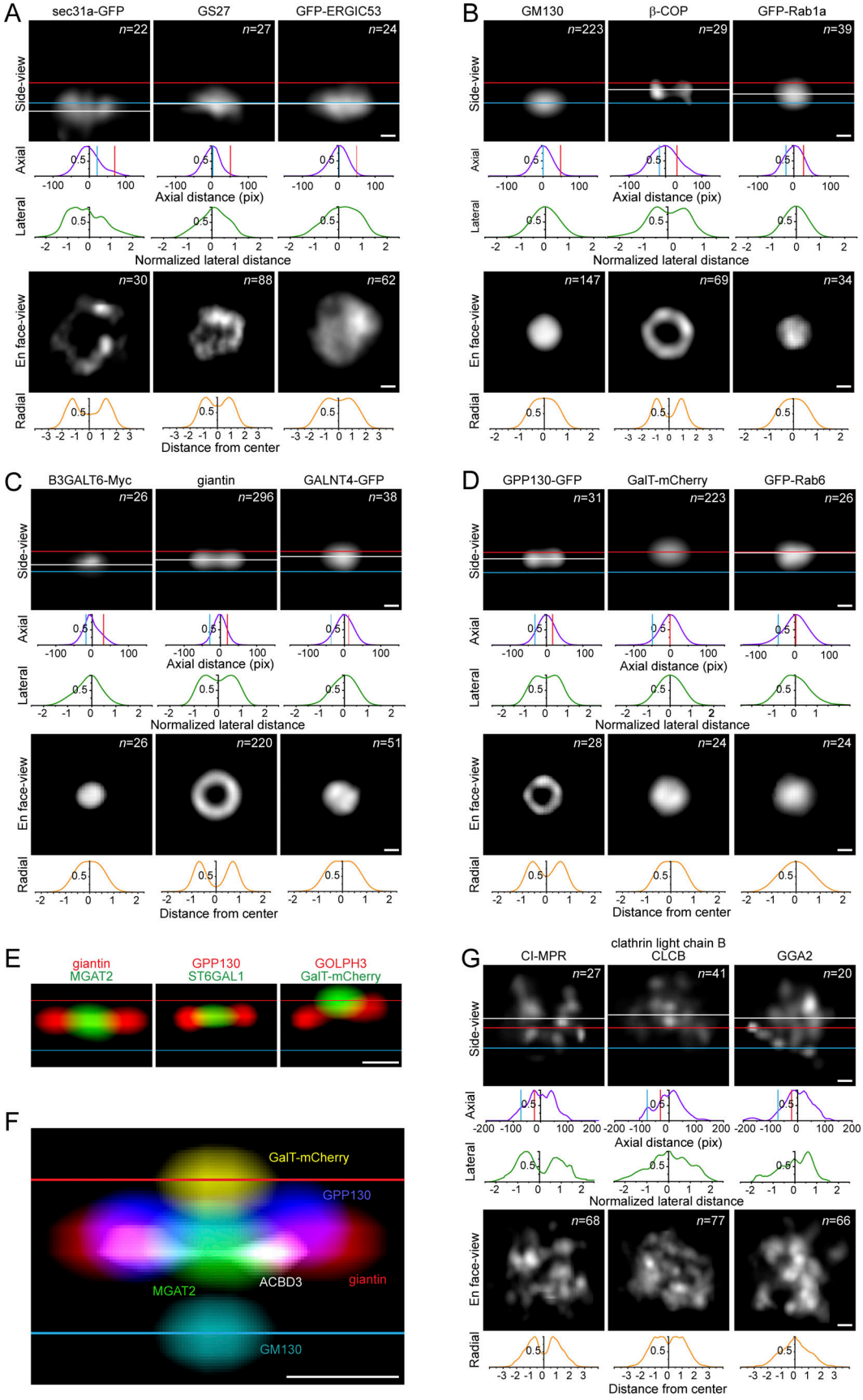

Figure 2. **Images and plots of side-averaged Golgi proteins.** HeLa cells expressing indicated exogenous proteins were nocodazole-treated and immunostained for giantin and the indicated proteins. **(A–D)** Side and en face averaged ERES and ERGIC ($LQ < -0.25$; A), *cis*-Golgi ($-0.25 \leq LQ < 0.25$; B), medial-

Golgi (0.25 ≤ *LQ* <0.75; C), and trans-Golgi proteins (0.75 ≤ *LQ* <1.25; D). In each panel, the first row shows side-average images. White, blue, and red horizontal lines represent fluorescence centers of the protein of interest, GM130, and GalT-mCherry, respectively. The second row shows the axial line intensity profile (Axial). The origin corresponds to the fluorescence center of the protein of interest. Intensity is normalized, and the unit of the axial distance is pixels. The third row shows the lateral line intensity profile (Lateral). Intensity is normalized, and the origin is at the Golgi axis. The *x* coordinate was normalized by half of the lateral size of giantin. The fourth row shows en face average images. The fifth row displays the radial mean intensity profile (Radial). The distance from the center was normalized by the radius of giantin. The number of ministacks analyzed, *n*, is indicated in the upper right corner of each average image. **(E and F)** Merged side-average images. Blue and red horizontal lines represent the fluorescence centers of GM130 and GalT-mCherry, respectively. **(G)** Side and en face averaged TGN proteins (*LQ* ≥ 1.25). Panels are organized as A–D. Proteins are arranged by their *LQ*s. Scale bar, 200 nm.

2009), although our GLIM supports its ERES localization (*LQ* = −0.81). The very asymmetrical and off-axial distribution of sec16a puncta could contribute to such a discrepancy. In summary, side-averaging supports and enhances our knowledge of the ministack, proving its validity as an imaging tool. Notably, it images the axial distribution of a Golgi protein, which no other optical methods currently can achieve according to our knowledge.

Modeling the molecular organization of the ministack

To suppress the morphological noise introduced by the small sample size, we took advantage of the symmetry of the ministack and performed reflection averaging. In this operation, side-averaged images were reflected about the Golgi axis and averaged with the original image (Materials and methods; Data S3). By merging selected reflection-averaged images (Fig. S3), a composite molecular image of the ministack, including the pre-Golgi region, was generated (Fig. 3 A). The composite image reinforced the stratum organization of the secretory processing unit, including the ERES, ERGIC, cis-to-trans cisternae, and TGN. It also highlighted the striking distributions of protein coats, including COPI (βCOP), COPII (sec31a-GFP), and clathrin coats (GFP-GGA1). GGA1-labeled clathrin coat appears to spread across a large area, capping the ministack like a crown at its trans-side, consistent with our knowledge that it decorates vesicles, buds, and tips of membrane tubules at the TGN (De Matteis and Luini, 2008; Guo et al., 2014). Both COPI (βCOP) and COPII distributions appear as a ring at the periphery of a ministack in en face views (Fig. 2, A and B). In the axial direction, COPI (βCOP) extends from the cis- to trans-cisternae, while the localization of COPII is distal to the cis-cisternae and away from COPI (βCOP). Our observation is consistent with previous reports on the tightly adjacent localization of COPII and COPI at the ER-proximal and distal region, respectively, near the ERES (Scales et al., 1997; Stephens et al., 2000; Weigel et al., 2021), and the cisternal rim distribution of COPI from the cis to trans-Golgi (Orci et al., 1997). Interestingly, we found that, in contrast to βCOP, γ1COP, one of the two paralogs of COPI's γ-subunit (Moelleken et al., 2007), localizes primarily from the pre-Golgi to the medial-Golgi in side-average (Fig. S2 B), as previously discovered under EM (Moelleken et al., 2007).

Combining our morphological and morphometric data, we made a table and schematic model to numerically and visually illustrate the molecular organization of an average Golgi ministack (Table 1 and Fig. 3 B). The axial position of a Golgi protein is linearly calculated as the product of its *LQ* and the axial size of the ministack, which was measured to be 274 nm (Fig. 1 A and Table 1). Hence, it has nanometer as the unit, and the axial position of GM130 is 0 nm. Similarly, the lateral sizes of Golgi proteins were converted to physical sizes (nm) using the product of normalized lateral sizes and the mean lateral size of giantin, 700 nm (Fig. 1 A and Table 1). In Fig. 3 B, cisternal diameters are approximated by the lateral sizes of cisternal rim markers, such as GM130, giantin, GPP130, and GOLPH3, components of the protein transport machinery. Furthermore, the membrane thickness (5 nm), the distance of the intracisternal (30 nm) and intercisternal (15 nm) membrane, and the diameter of a vesicle/bud (60 nm) are roughly drawn in scale according to published EM data (Ladinsky et al., 1999; Trucco et al., 2004). Hence, the distance from the cis to the trans side of a ministack (*LQ* from −0.25 to 1.25) has roughly seven cisternae, calculated by the above morphometric parameters. The number of cisternae per ministack, seven, is consistent with the 3D EM tomography data acquired in NRK cells (Ladinsky et al., 1999). Our table and model should further help to understand the molecular organization of the Golgi.

Imaging intra-Golgi transport of secretory cargos

Using side-averaging, we investigated intra-Golgi trafficking of secretory cargos. We adopted the retention using selective hooks (RUSH) system to synchronously release a cargo into the secretory pathway (Boncompain et al., 2012). After administering biotin and cycloheximide (CHX; to stop protein synthesis) in the nocodazole-treated cells, VSVG-SBP-GFP (hereafter referred to as VSVG) was released to the secretory pathway from the ER to the Golgi en route to the PM. As we previously observed using VSVGtso45-GFP (Tie et al., 2016), the *LQ*- or LQ^{side}-vs.-time plot demonstrated that the VSVG traffic wave rapidly transited through the ministack and remained at the trans-Golgi for a prolonged time before disappearance (Fig. 4, A and B). Side-averaging enabled direct visualization of such cisternal transition of VSVG from the cis- to the trans-Golgi, where it appeared stationary until it disappeared at the ministack due to the exocytic trafficking (first row of Fig. 4 C). The length of time that VSVG pauses at the trans-Golgi is indicated by its Golgi residence time, which can be measured by the half-life of the Golgi fluorescence decay after the release of 20°C block (Sun et al., 2021; Sun et al., 2020). We have recently measured the Golgi residence time of VSVG to be 12 min. Furthermore, we found that different constitutive transmembrane secretory cargos have distinct Golgi residence times, which are determined by their Golgi export signals, such as the linked glycan, the transmembrane domain, and the cytosolic tail (Sun et al., 2021; Sun et al., 2020).

Throughout the intra-Golgi transport, VSVG maintained a unimodal and synchronous trafficking wave (second row of Fig. 4 C), consistent with the previous EM study (Trucco et al.,

Table 1. **Morphometric parameters of Golgi proteins in an average ministack**

Name	GLIM			Side-averaging				
	LQ	SEM	*n*	LQ^{side}	*n*	Axial position (nm)	Normalized lateral size	Lateral size (nm)
mGFP-sec16a	−0.81	0.12	79	0.04	39	12	0.80	563
sec31a-GFP	−0.65[a]	0.06	67	−0.43	22	−118	1.16	810
sec23a-mCherry	−0.58[b]	0.06	121	−0.30	37	−82	0.98	690
GS27	−0.22[a]	0.03	101	−0.06	27	−17	0.71	500
γ1COP	−0.17[b]	0.07	106	0.18	26	48	1.10	770
GFP-ERGIC53	−0.16[a]	0.02	198	−0.05	24	−12	0.90	630
GM130	0.00[c]			0.00	223	0	0.64	450
βCOP	0.15	0.06	183	0.45	29	122	1.11	784
GFP-Rab1a	0.21[b]	0.03	154	0.43	39	119	0.57	400
GFP-ACBD3	0.25[b]	0.03	132	0.51	32	139	0.72	506
VIP36-GFP	0.30	0.02	134	0.26	17	71	0.64	450
GALNT8-GFP	0.34	0.05	73	0.28	21	78	0.61	430
B3GALT6-Myc	0.47[b]	0.03	97	0.33	16	90	0.61	430
B4GALT7-Myc	0.52[b]	0.04	110	0.14	19	39	0.64	450
MGAT2-Myc	0.53[b]	0.04	136	0.50	34	138	0.55	380
Giantin	0.57[b]	0.05	103	0.58	73	160	1.00	700
GALNT4-GFP	0.58	0.02	163	0.74	38	203	0.60	420
TPST2-GFP	0.64[b]	0.02	154	0.66	47	180	0.54	380
POMGNT1-Myc	0.67[b]	0.04	87	0.76	30	209	0.61	430
GCNT1-GFP	0.69	0.03	167	0.83	25	226	0.75	520
B4GALT3-Myc	0.74[b]	0.02	149	0.78	42	215	0.59	410
TPST1-GFP	0.76[a]	0.04	111	0.95	30	260	0.58	400
GPP130-GFP	0.84[a]	0.02	168	0.65	31	178	0.90	630
SLC35C1-Myc	0.84[b]	0.04	85	0.95	18	259	0.68	479
ST6GAL1-GFP	0.85[b]	0.02	138	0.71	35	195	0.67	470
GalT-mCherry	1.00[b]			1.00	223	274	0.67	470
GFP-Rab6	1.04[a]	0.04	262	0.95	26	260	0.76	530
GFP-GOLPH3	1.05	0.03	99	0.80	20	220	0.87	610
GFP-GGA1	1.30[a]	0.12	33	1.54	18	423	1.75	1,220
GFP-golgin-97	1.45[b]	0.03	161	1.33	26	364	0.63	440
CI-M6PR	1.46[b]	0.24	42	1.47	27	403	1.35	940
Cab45-Myc	1.49	0.07	96	1.13	22	308	0.76	530
Vamp4-GFP	1.57[a]	0.04	157	1.47	16	402	0.66	470
Furin-GFP	1.64	0.08	55	1.69	28	463	0.64	450
CLCB	1.65[b]	0.26	37	1.66	41	455	1.66	1,160
SMS1-Myc	1.76	0.08	105	1.51	28	414	0.59	410
GGA2	1.96[a]	0.23	33	1.48	20	405	1.35	950
γ-Adaptin	2.20	0.14	43	1.60	18	438	1.62	1,140

Data are calculated from GLIM and side-averaging, assuming that the Golgi ministack has an average size. In GLIM and side-averaging, *n* represents the number of ministacks analyzed.
[a]Data from Tie et al. (2016).
[b]Data from Tie et al. (2018).
[c]By definition.

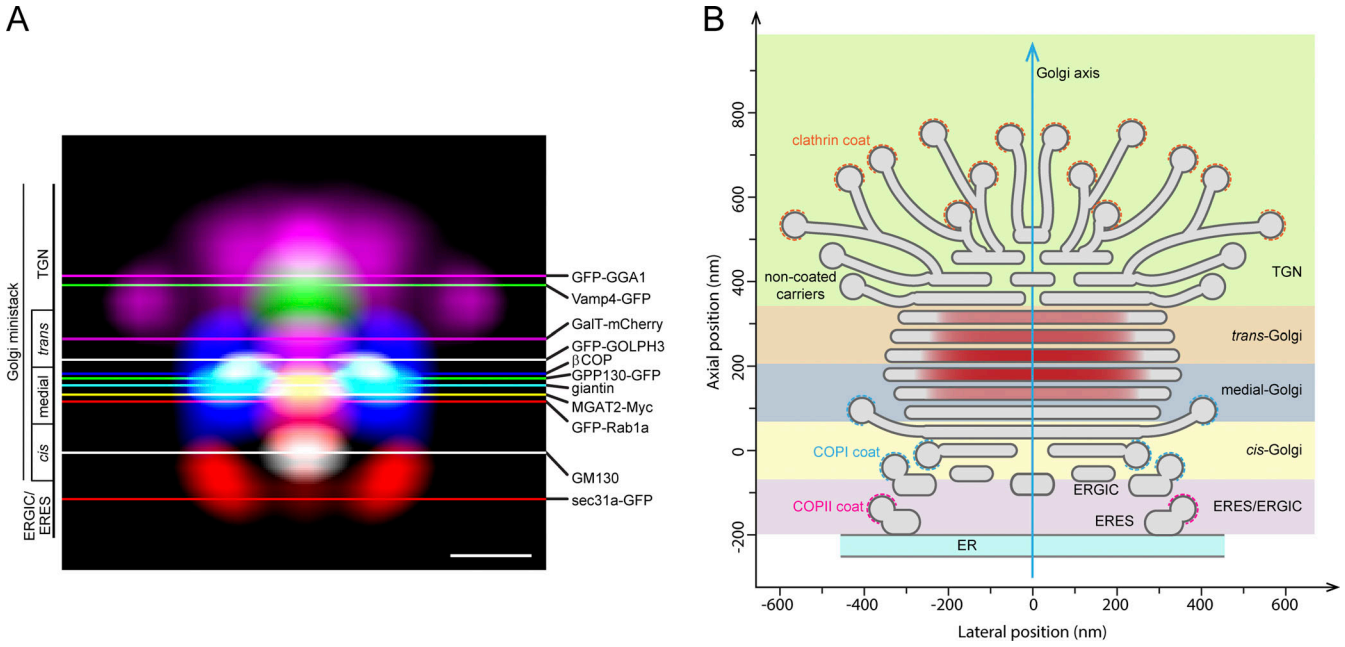

Figure 3. **A model of the Golgi ministack. (A)** The composite image of side-averaged Golgi proteins demonstrating the organization of the Golgi ministack. Selected side-average images of Golgi proteins were further reflection-averaged (Fig. S3) and merged. Scale bar, 200 nm. **(B)** A schematic diagram of an average Golgi ministack. The diagram was constructed roughly to the scale according to our side-average data and the composite image in A. The unit in the x and y axis is nm. 0 nm in the x and y axis corresponds to the Golgi axis and the fluorescence center of GM130 (*LQ* = 0), respectively. The maximal lateral size of the stacked cisternae is 700 nm, corresponding to that of giantin. The axial size of the ministack is 274 nm. The axial positions of ERES/ERGIC, cis, medial, trans, and TGN regions were calculated by multiplying their *LQ* intervals, (−∞, −0.25), [−0.25, 0.25), [0.25, 0.75), [0.75, 1.25], and [1.25, ∞), respectively, with one unit of *LQ* (the axial distance from GM130 to GalT-mCherry), which is 274 nm.

2004) and suggesting that it should not homogeneously distribute across the ministack. Interestingly, en face averaging showed that the diameter of the VSVG traffic wave first increased (0–15 min) and then decreased (15–20 min) during its transition through the ministack (fourth row of Fig. 4, C and D). However, we found that the diameter of VSVG was always smaller than those of corresponding rim markers (Fig. 4 D), consistent with the interior localization of secretory cargos, as we previously reported (Tie et al., 2018). Therefore, our data imply that the cisternal interior, accessible to VSVG during its Golgi transition, might vary proportionally to the cisternal diameter.

The same experiment was also conducted for the GPI-anchored constitutive secretory cargo—CD59 (Fig. S4). Similarly, together with the *LQ*- and LQ^{side}-vs.-time plots, side-averaging directly demonstrated the rapid cisternal transition of CD59 from the cis- to the trans-Golgi and eventual exit at the trans-Golgi (Fig. S4, A–C). However, the newly synthesized TGN protein, such as CD8a-furin, reached the TGN (Fig. 4, E–G) via the secretory pathway, as we previously reported (Tie et al., 2016). The tyrosine (Y)-based or acidic cluster (AC)-based motif in the cytosolic tail has been demonstrated to be sufficient for the secretory TGN-targeting of furin (Tie et al., 2016). Consistent with this view, when both motifs were mutated, the resulting mutant, CD8a-furin (Y + AC), failed to reach the TGN (Fig. 4, H–J). Instead of the TGN, it exited the ministack at the trans-Golgi (Fig. 4, H–J), similar to the constitutive secretory cargos such as VSVG and CD59. Hence, our side-averaging method provided visual images to support that the secretory TGN targeting is signal dependent, a notion that we previously deduced from GLIM (Tie et al., 2016).

The cisternal localization of VSVG at 15° and 20°C

15° or 20°C incubation is commonly believed to selectively arrest the secretory cargos, such as VSVG, at the ERGIC and trans-Golgi/TGN, respectively (Matlin and Simons, 1983; Saraste and Kuismanen, 1984). However, the view has not been substantiated by direct and systematical sub-Golgi imaging in the context of well-defined cisternal markers. Previously, we employed GLIM to demonstrate that ER-synchronized VSVGts045-GFP is arrested at the pre- and medial-Golgi under 15° and 20°C incubation, respectively (Tie et al., 2016). When VSVG RUSH reporter was released from the ER at 15°C for 2 h, side-averaging revealed that its traffic wave stopped at a pre-Golgi position in between sec23a-mCherry (LQ^{side} = −0.30) and GS27 (LQ^{side} = −0.06) with the LQ^{side} = −0.23 (Fig. 5 A), consistent with the EM result in NRK ministacks (Trucco et al., 2004). At 20°C, on the other hand, VSVG traffic wave was arrested at the medial-Golgi, instead of the trans-Golgi or the TGN, in between MGAT2-Myc (LQ^{side} = 0.50) and giantin (LQ^{side} = 0.58) with the LQ^{side} = 0.52 (Fig. 5 B). Like intra-Golgi transport, we noted that the axial line intensity profile of VSVG remained unimodal under both temperature blocks (Fig. 5, A and B), suggesting that VSVG should not distribute homogeneously across the ministack. The finding was consistent with our *LQ* data using VSVGts045-GFP (Tie et al., 2016), but at odds with the generally believed trans-Golgi/TGN localization at 20°C.

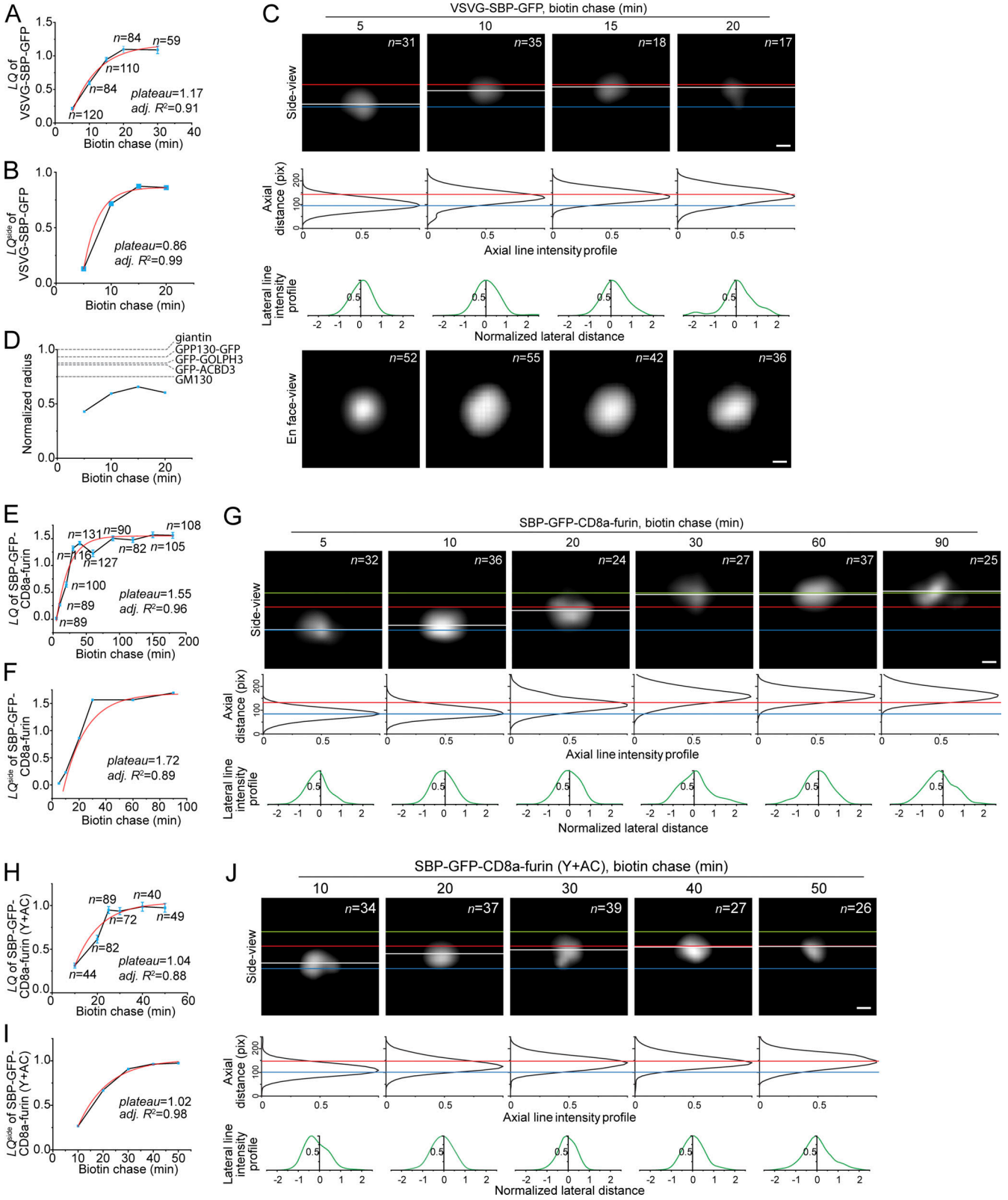

Figure 4. **Imaging intra-Golgi secretory transport by side-averaging. (A–D)** The intra-Golgi transport of VSVG by side-averaging. HeLa cells transiently coexpressing GalT-mCherry and the RUSH reporter, VSVG-SBP-GFP, were first incubated with nocodazole to induce the formation of ministacks. Cells were subsequently treated with biotin and CHX in the presence of nocodazole to chase VSVG-SBP-GFP along the secretory pathway. Cells were fixed and immunostained for endogenous GM130 to acquire the *LQ* of VSVG-SBP-GFP (A). In the *LQ*-vs.-time plot, the data points are colored blue. Error bar, mean ± SEM. *n*, the number of ministacks analyzed. Data were fitted to the first-order exponential decay function (red line). The plateau and adjusted R^2 (adj. R^2) are from the fitting. Alternatively, fixed cells were immunostained for endogenous giantin to side-average VSVG-SBP-GFP. In B, LQ^{side} values were acquired from side-

average images and are colored blue. Similar to A, LQ^{side}-vs.-time plot was fitted to the first-order exponential decay function. In C, the panel is organized as in Fig. 2, A–D. The exception is the second row, in which axial line intensity plots are presented with the x and y axis swapped. In D, the normalized radius against time plot shows the change of the radius of VSVG-SBP-GFP during its intra-Golgi transport. Normalized radii were calculated using the radial mean intensity profile of the corresponding en face average images. **(E–J)** The intra-Golgi transport of SBP-GFP-CD8a-furin WT (E–G) and Y + AC mutant (H–J) by side-averaging. The experiments and the organization of panels are similar to those in A–C. Horizontal green lines in G and J represent the axial position of CLCB. In C, G, and J, scale bars, 200 nm.

Discussion

The Golgi stack has diverse appearances under EM and light microscopy. The morphology of the nocodazole-induced Golgi ministack appears to be more uniform but still displays substantial variations. Multiple factors contribute to the variation in addition to the spatial orientation of the ministack. For example, the ministack is well known to be highly dynamic with constant membrane extension, budding, and fusion. Furthermore, mechanical forces from the cytoskeleton might change the apparent shape of the ministack. The morphological variation can be considered as noise in imaging the cisternal organization of the Golgi. Averaging normalized and aligned ministacks should effectively suppress the morphological noise, enhancing their intrinsic structural features.

We demonstrated that our side-averaging method can reveal the axial and lateral distribution of a Golgi protein. By this approach, we directly visualized and analyzed the axial distribution of >30 Golgi proteins. The lateral distribution revealed by side-averaging is consistent with the data acquired via GLIM, en face averaging, and EM results from the literature review. Furthermore, side-averaging enabled us to generate a rough physical map of the ministack. Most importantly, it imaged the rapid and progressive intra-Golgi transport of secretory cargos

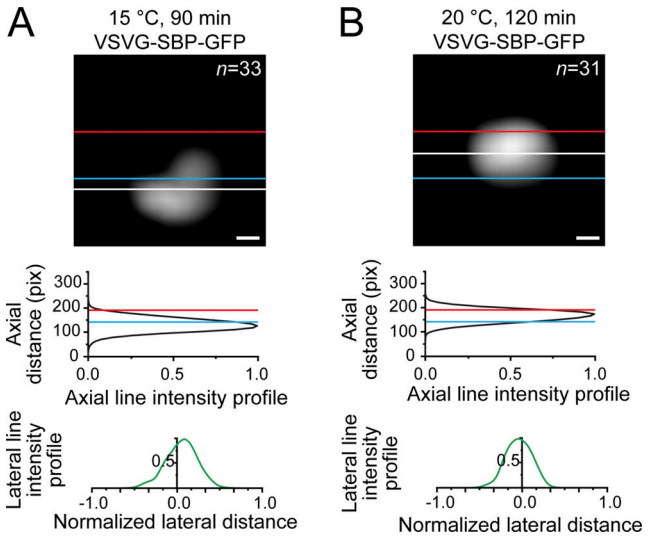

Figure 5. **Imaging the intra-Golgi transport of VSVG under 15° and 20°C temperature block.** HeLa cells transiently expressing the RUSH reporter, VSVG-SBP-GFP, were first incubated with nocodazole to induce the formation of ministacks. **(A and B)** Cells were subsequently treated with biotin and CHX in the presence of nocodazole at 15°C (A) or 20°C (B) for 90 or 120 min, respectively. Cells were fixed and immunostained for endogenous giantin before side-averaging. The organization of panels is similar to that of Fig. 4 C. Scale bar, 200 nm.

such as VSVG, CD59, and CD8a-furin. Our imaging data demonstrated the prolonged pause of newly synthesized VSVG, CD59, and CD8a-furin (Y + AC) traffic waves at the trans-Golgi before the disappearance. In contrast, a newly synthesized CD8a-furin traffic wave reached the TGN and localized there at the steady-state. Therefore, our data support our previous model in which the trans-Golgi acts as the exit site for the constitutive secretory cargos, and the secretory TGN targeting is signal-dependent (Tie et al., 2016). However, our data do not agree with the prevailing model, which posits the TGN as the Golgi exit site of the constitutive secretory cargos (De Matteis and Luini, 2008; Di Martino et al., 2019).

Our model agrees with several EM tomography studies using cryofixation (Ladinsky et al., 1999; Marsh et al., 2001; Mogelsvang et al., 2004). The 3D tomographic organization of the Golgi demonstrates that the trans-most cisternae generate a clathrin-positive tubular and vesicular membrane network characterizing the TGN. Furthermore, it uncovers that the two adjacent trans-cisternae assemble clathrin-negative vesicles and tubules representing the constitutive secretory carriers, supporting our model that constitutive secretory cargos can exit at the trans-Golgi. However, we can not rule out the possible scenario where cargos might transit through the TGN so rapidly that their presence in the TGN is undetectable under our imaging condition. If the scenario is true, we argue that it would have been impossible for EM to detect cargo's presence in the TGN either. Another scenario is that the Golgi-associated microtubule cytoskeleton, which is depolymerized in our imaging, could play an essential role in positioning the Golgi exit site. Therefore, further high-speed and high-sensitivity live-imaging of the native Golgi is necessary to resolve these two models. Despite these caveats, the most straightforward explanation to our data is that constitutive secretory cargos exit at the trans-Golgi instead of the TGN.

The molecular and cellular mechanism on intra-Golgi transport is still unclear, primarily due to the challenge in imaging the highly dynamic movement of cargos within tightly spaced Golgi cisternae. Three major intra-Golgi transport models have been proposed and are currently under debate (Glick and Luini, 2011). (1) The cisternal maturation or progression model proposes that a Golgi cisterna is a transient entity. According to this view, secretory cargos are passively carried within cisternae. Their intra-Golgi transport occurs when Golgi cisternae continuously mature to the next stage along the cis-to-trans Golgi axis. (2) In contrast, the stable compartment or vesicular transport model hypothesizes that Golgi cisternae are stable entities. The intra-Golgi secretory transport is mediated by vesicles, which sequentially carry cargos from one cisterna to the next along the Golgi axis. (3) The recently proposed rapid

partitioning model states that secretory cargos are rapidly mixed throughout the Golgi upon entry and subsequently separated into numerous processing and export domains. Now, the maturation model is best received after the direct imaging of the cis-to-trans cisternal transition in the budding yeast (Losev et al., 2006; Matsuura-Tokita et al., 2006). Our side-averaging directly revealed the progressive shift of the secretory cargos from the cis to the trans-Golgi in mammalian cells. Furthermore, during the intra-Golgi transport, our RUSH cargos remain a synchronous traffic wave with a unimodal axial distribution. Our observation hence agrees with the prediction of the cisternal maturation and stable compartment models. However, it is at odds with that of the rapid partitioning model, in which secretory cargos rapidly and homogenously partition throughout the Golgi stack (Patterson et al., 2008). More robust experimental evidence, especially imaging evidence, is required to evaluate these models further.

Our side-averaging method makes it possible to resolve the dynamic intra-Golgi transport using commonly available light microscopy, such as Airyscan and 3D-structured illumination microscopy. Thus, we believe that side-averaging, together with GLIM and en face averaging, would be an invaluable tool in exploring the molecular and cellular mechanisms behind Golgi trafficking.

Materials and methods

DNA plasmids

Sec31a-GFP (Tang et al., 2000), sec23a-mCherry, GFP-golgin-97 (Lu et al., 2006), and Vamp4-GFP (Tran et al., 2007) were gifts from W. Hong. GFP-ERGIC53 (Ben-Tekaya et al., 2005) was a gift from H. Hauri. GPP130-GFP (Linstedt et al., 1997) was a gift from A. Linstedt. Strep-Ii_VSVG-SBP-GFP (Boncompain et al., 2012) was a gift from F. Perez. Cab45-Myc (von Blume et al., 2012) was a gift from J. von Blume. mGFP-sec16a (#15776; Addgene; Bhattacharyya and Glick, 2007) was a gift from B. Glick. TPST1-GFP and TPST2-GFP (Spooner et al., 2008) were gifts from D. Stephens. Strep-KDEL_ss-SBP-GFP-CD8a-furin (WT), Strep-KDEL_ss-SBP-GFP-CD8a-furin (Y + AC), Strep-KDEL_ss-SBP-GFP-CD59, and GalT-mCherry were previously described (Tie et al., 2016). GFP-Rab6, ST6GAL1-GFP, ST6GAL1-Myc, GFP-Rab1a, MGAT2-Myc, GFP-ACBD3, B4GALT3-Myc, GFP-GGA1, and furin-GFP were previously described (Tie et al., 2018). B4GALT7-Myc (#RC200258), B3GALT6-Myc (#MR204731), POMGNT1-Myc (#RC200176), SLC35C1-Myc (#RC200101), and SMS1-Myc (#MR206639) were purchased from Origene. Cloning methods for constructing VIP36-GFP, GALNT8-GFP, GALNT4-GFP, GCNT1-GFP, and GFP-GOLPH3 are described in Table S3.

Antibodies and small molecules

Mouse mAbs against GS27 (#611034; immunofluorescence [IF] dilution 1:250), GM130 (#610823; IF dilution 1:500) and GGA2 (#612612; IF dilution 1:200) were from BD Bioscience. Mouse mAbs against Myc (#9E10; IF dilution 1:200), βCOP (#SC-393615; IF dilution 1:200), γ1COP (#SC-393977; IF dilution 1:200), and CLCB (#SC-376414; IF dilution 1:200) were from Santa Cruz. Mouse mAb against CI-M6PR (#MA1-066; IF dilution: 1:200) and rabbit polyclonal antibody against furin (#PA1062; IF dilution 1:100) were from Thermo Fisher Scientific. Rabbit polyclonal antibody against giantin (#924302; IF dilution 1:1,000) was from BioLegend. Mouse mAb against γAdaptin (#A4200; IF dilution 1:250) was from Sigma-Aldrich. Goat secondary antibodies against mouse IgG conjugated with Alexa Fluor 647 (#A21235), 594 (#A11005), and 488 (#A11001); goat secondary antibodies against rabbit IgG conjugated with Alexa Fluor 594 (#A11012) and 488 (#A11008); and donkey secondary antibody against mouse IgG conjugated with Alexa Fluor Plus 680 (#A32788) were from Invitrogen. The IF dilutions for all secondary antibodies were 1:500. Nocodazole (#487928) was from Merck, and its working concentration was 33 µM. Biotin was from IBA Lifesciences (#21016002), and its working concentration was 40 µM. CHX was from Sigma-Aldrich (#C1988), and its working concentration was 10 µg/ml.

Cell culture, transfection, and immunofluorescence labeling

HeLa cells were from American Type Culture Collection and cultured in DMEM supplemented with 10% FBS. Cells were grown on Φ 12-mm and no. 1.5 glass coverslips. The transient transfection was conducted using Lipofectamine 2000 according to the manufacturer's protocol. In all imaging experiments, cells were treated with 33 µM nocodazole for 3 h before further treatment.

IF labeling was performed as described previously (Tie et al., 2016). Briefly, cells grown on the glass coverslip were fixed with 4% PFA in PBS, followed by washing with 100 mM NH_4Cl. Next, cells were sequentially incubated with primary and fluorescence-conjugated secondary antibodies diluted in an antibody dilution buffer (2% FBS, 2% BSA, and 0.1% saponin in PBS). After extensive washing with PBS, cells were mounted onto a glass slide in the Mowiol mounting medium, consisting of 12% Mowiol 4-88 (#475904; Calbiochem), 30% glycerol, and 100 mM Tris, pH 8.5.

Airyscan microscopy

Airyscan microscopy was conducted on a Zeiss LSM710 confocal microscope equipped with α Plan-Apochromat 100× NA 1.46 objective, a motorized stage, a temperature-controlled environment chamber, and the Airyscan module (Carl Zeiss). Three lines of laser lights were used, 488, 561, and 640 nm. The emission band was selected to maximize the collection of the emission light while avoiding channel crosstalk. The system was controlled by Zen software (Carl Zeiss). The pixel size of our images is 45 nm. Chromatic shift aberration was not considered, as the shift in all directions is <20 nm.

Wide-field microscopy

*LQ*s were acquired by a conventional wide-field microscope comprising Olympus IX83 equipped with an oil objective lens (100×, NA 1.40), a motorized staged, motorized filter cubes, an sCMOS (scientific complementary metal oxide semiconductor) camera (Neo; Andor), and a 200W metal-halide excitation light source (Lumen Pro 200; Prior Scientific). Dichroic mirrors and filters were optimized for GFP/Alexa Fluor 488, mCherry/Alexa Fluor 594, Alexa Fluor 647, and Alexa Fluor plus 680. The system was controlled by Metamorph software (Molecular Devices).

Intra-Golgi secretory transport of RUSH reporters

HeLa cells were transiently transfected to express GalT-mCherry and a RUSH reporter and were cultured in the presence of 16 nM His-tagged streptavidin. After 3 h of nocodazole treatment, 40 µM biotin and 10 µg/ml CHX were added to the medium, and cells were chased for various lengths before fixation and immunostained for giantin (for side or en face averaging) or endogenous GM130 (for the acquisition of *LQ*). The side- and en face–view images were acquired from the Airyscan microscope. The *LQ* of the RUSH reporter was acquired via wide-field microscopy.

Calculation of the *LQ*

HeLa cells transiently expressing GalT-mCherry were treated with nocodazole for 3 h and subsequently triple-labeled to reveal endogenous GM130, transfected GalT-mCherry, and the protein of interest, which was either endogenous or transfected. Ministacks were imaged under a wide-field microscope. The subsequent analysis was conducted as previously described (Tie et al., 2017; Tie et al., 2016). Briefly, ministacks were first manually selected. Next, fluorescence centers of GM130, GalT-mCherry, and the protein of interest were acquired in Fiji (https://imagej.net/software/fiji/). After correcting the chromatic aberration, coordinates of fluorescence centers were used to calculate the *LQ*, which is the ratio of the axial distance from GM130 to the protein of interest and that from GM130 to GalT-mCherry (Tie et al., 2017; Tie et al., 2016). Fitting of *LQ* (including LQ^{side}) data to the first-order exponential decay function was performed in OriginPro2020.

Side-averaging

HeLa cells transfected or not were treated with nocodazole for 3 h before fixation and immunostaining for endogenous giantin and Golgi proteins of interest if they were not tagged by a fluorescence protein. Multichannel images were subsequently acquired using Airyscan microscopy. Acquired images were examined in Fiji. Ministacks showing side-views were identified by the giantin double-punctum appearance. We exhausted an image to select all ministacks showing side-views. Each ministack side-view was first cropped to a minimal square and background-subtracted. Irrelevant fluorescent objects in the image were manually removed in Fiji (Edit > Clear). Based on the co-stained Golgi marker(s), the side-view was then rotated or flipped (Image > Transform: Flip or Rotate) so that the trans-side of the Golgi was up. Next, two regions of interest (ROIs) were manually drawn to mark the left and right giantin punctum and imported to the ROI manager. With both ROIs deselected and the giantin channel selected as the active one, the macro program "P1-Rotate_Resize_Normalize" (Data S1) was executed. After that, the processed images were retrieved from the designated folder and subjected to averaging in Fiji (Image > Stacks > Z Project: Average Intensity). The resulting average is further processed by the macro program "P2-Resize_Add_Line" (Data S2) to make the image isotropic in scale. The pixel size of our side-average images is 5.6 nm. Selected side-average images were further reflection-averaged by the macro "P3-Reflection_Average" (Data S3).

Morphometric analysis of side-average images of Golgi proteins

Analysis of side-average images was conducted in Fiji (https://imagej.net/software/fiji/). Table S1 lists all morphometric variables defined or used in this study. A line was drawn along the x or y axis to acquire the lateral or axial line intensity profiles, respectively (Fig. S1, B and C). The thickness of the line was sufficiently large to include all the intensity signals. The axial line intensity plot of a Golgi protein has a single peak. In Fig. 1, A–D, the axial line intensity profile of GM130, giantin, or GalT-mCherry was subjected to Gaussian fitting in OriginPro2020 (analysis > fitting > non-linear curve fit). The calculated *Xc* represents the axial position of the protein. Except for Fig. 1, A–D, the axial position was calculated as the *y* coordinate of the fluorescence center.

The lateral line intensity profile of a rim-localized Golgi protein has two peaks. They were fitted to the two-peak Gaussian function in OriginPro2020 (analysis > peak and baseline > multiple peak fit). The lateral size of giantin was defined as the distance between the half-maxima of the outer slopes. It was calculated as $(Xc_2 - Xc_1 + 0.5 \times w_1 + 0.5 \times w_2)$, in which Xc_1, Xc_2, w_1, and w_2 are from the two-peak Gaussian fitting. The lateral sizes of other rim-localized proteins, such as ACBD3, GPP130, and GOLPH3, were similarly acquired. The lateral width of giantin punctum was defined as the mean of the two FWHMs of puncta. It was calculated as $0.5 \times (w_1 + w_2)$, in which w_1 and w_2 are from the two-peak Gaussian fitting in OriginPro2020. Lateral line intensity profiles of interior-localized proteins have a broad peak. They were fitted to the super-Gaussian function, and the resulting FWHMs were used as their lateral sizes.

En face averaging

HeLa cells were treated with nocodazole for 3 h and immunostained to reveal endogenous giantin and the protein of interest, either endogenous or transfected. Images were acquired under the Airyscan microscope. En face views of ministacks were identified by the ring appearance of giantin. En face averaging and the radial mean intensity profile were previously described (Tie et al., 2018). The radius is defined as the distance from the half-maximum position of the outer slope to the center. In the radial mean intensity profile, the x axis (distance from center) is normalized by the radius of giantin. The normalized radius of a Golgi protein is its radius divided by that of giantin. To ensure that our en face average has the same pixel size as the side-average, which is 5.6 nm/pixel, we multiplied the number of pixels along the width and height of our en face average with a fixed factor, 0.514, in Fiji (image > adjust > size: bilinear). After this adjustment, the diameters of giantin in the en face and side-average images should have the same value, 700 nm. In Figs. 2 and S2, the following en face average images were adopted and modified from our previous work (Tie et al., 2018): GM130, GFP-Rab1a, B3GALT6-Myc, giantin, GPP130-GFP, GFP-Rab6, GalT-mCherry, GFP-ACBD3, ST6GAL1-Myc, TPST1-GFP, SLC35C1-Myc, B4GALT7-Myc, MGAT2-Myc, TPST2-GFP, and POMGNT1-Myc.

Online supplemental material

Fig. S1 shows the giantin distribution among ministacks, morphometric parameters of a side-view ministack, and the effect of

overexpression on the *LQ*. Fig. S2 shows images and plots of side-averaged Golgi proteins. Fig. S3 shows images of reflection-averaged Golgi proteins used in Fig. 3 A. Fig. S4 shows the intra-Golgi secretory transport of CD59 by side-averaging. Table S1 lists terms and variables defined or used in this study. Table S2 compares side-average data with corresponding published EM localization results. Table S3 lists DNA plasmids constructed in this study. Data S1 shows the code for the Fiji macro "P1-Rotate_Resize_Normalize." Data S2 shows the code for the Fiji macro "P2-Resize_Add_Line." Data S3 shows the code for the Fiji macro "P3-Reflection_Average."

Acknowledgments

We thank B. Glick (University of Chicago), H. Hauri (University of Basel, Switzerland), W. Hong (Institute of Molecular and Cell Biology, Singapore), A. Linstedt (Carnegie Mellon University), F. Perez (Institute Curie, France), D. Stephens (University of Bristol, UK), and J. von Blume (Yale School of Medicine) for sharing DNA plasmids, and R. Guiet and O. Burri (EPFL, Switzerland) for providing super-Gaussian fitting Fiji macro.

The following grants to L. Lu supported this work: MOE AcRF Tier1 RG35/17, Tier2 MOE2015-T2-2-073, and MOE2018-T2-2-026.

The authors declare no competing financial interests.

Author contributions: Conceptualization: L. Lu. Formal analysis: H.C. Tie, D. Mahajan, and L. Lu. Investigation and data curation: H.C. Tie and D. Mahajan. Software, supervision, and writing – original draft: L. Lu. Writing – review & editing: L. Lu, H.C. Tie, and D. Mahajan.

Submitted: 24 September 2021
Revised: 3 December 2021
Accepted: 5 April 2022

References

Antony, C., C. Cibert, G. Geraud, A. Santa Maria, B. Maro, V. Mayau, and B. Goud. 1992. The small GTP-binding protein rab6p is distributed from medial Golgi to the trans-Golgi network as determined by a confocal microscopic approach. *J. Cell Sci.* 103:785–796. https://doi.org/10.1242/jcs.103.3.785

Bell, A.W., M.A. Ward, W.P. Blackstock, H.N. Freeman, J.S. Choudhary, A.P. Lewis, D. Chotai, A. Fazel, J.N. Gushue, J. Paiement, et al. 2001. Proteomics characterization of abundant Golgi membrane proteins. *J. Biol. Chem.* 276:5152–5165. https://doi.org/10.1074/jbc.M006143200

Ben-Tekaya, H., K. Miura, R. Pepperkok, and H.P. Hauri. 2005. Live imaging of bidirectional traffic from the ERGIC. *J. Cell Sci.* 118:357–367. https://doi.org/10.1242/jcs.01615

Bhattacharyya, D., and B.S. Glick. 2007. Two mammalian Sec16 homologues have nonredundant functions in endoplasmic reticulum (ER) export and transitional ER organization. *Mol. Biol. Cell.* 18:839–849. https://doi.org/10.1091/mbc.e06-08-0707

Boncompain, G., S. Divoux, N. Gareil, H. de Forges, A. Lescure, L. Latreche, V. Mercanti, F. Jollivet, G. Raposo, and F. Perez. 2012. Synchronization of secretory protein traffic in populations of cells. *Nat. Methods.* 9:493–498. https://doi.org/10.1038/nmeth.1928

Bosshart, H., J. Humphrey, E. Deignan, J. Davidson, J. Drazba, L. Yuan, V. Oorschot, P.J. Peters, and J.S. Bonifacino. 1994. The cytoplasmic domain mediates localization of furin to the trans-Golgi network en route to the endosomal/lysosomal system. *J. Cell Biol.* 126:1157–1172. https://doi.org/10.1083/jcb.126.5.1157

Bottanelli, F., E.B. Kromann, E.S. Allgeyer, R.S. Erdmann, S. Wood Baguley, G. Sirinakis, A. Schepartz, D. Baddeley, D.K. Toomre, J.E. Rothman, and J. Bewersdorf. 2016. Two-colour live-cell nanoscale imaging of intracellular targets. *Nat. Commun.* 7:10778. https://doi.org/10.1038/ncomms10778

Chen, X., E.S. Simon, Y. Xiang, M. Kachman, P.C. Andrews, and Y. Wang. 2010. Quantitative proteomics analysis of cell cycle-regulated Golgi disassembly and reassembly. *J. Biol. Chem.* 285:7197–7207. https://doi.org/10.1074/jbc.M109.047084

Cole, N.B., N. Sciaky, A. Marotta, J. Song, and J. Lippincott-Schwartz. 1996. Golgi dispersal during microtubule disruption: Regeneration of Golgi stacks at peripheral endoplasmic reticulum exit sites. *Mol. Biol. Cell.* 7:631–650. https://doi.org/10.1091/mbc.7.4.631

De Matteis, M.A., and A. Luini. 2008. Exiting the Golgi complex. *Nat. Rev. Mol. Cell Biol.* 9:273–284. https://doi.org/10.1038/nrm2378

Dejgaard, S.Y., A. Murshid, K.M. Dee, and J.F. Presley. 2007. Confocal microscopy-based linescan methodologies for intra-Golgi localization of proteins. *J. Histochem. Cytochem.* 55:709–719. https://doi.org/10.1369/jhc.6A7090.2007

Di Martino, R., L. Sticco, and A. Luini. 2019. Regulation of cargo export and sorting at the trans-Golgi network. *FEBS Lett.* 593:2306–2318. https://doi.org/10.1002/1873-3468.13572

Doray, B., P. Ghosh, J. Griffith, H.J. Geuze, and S. Kornfeld. 2002. Cooperation of GGAs and AP-1 in packaging MPRs at the trans-Golgi network. *Science.* 297:1700–1703. https://doi.org/10.1126/science.1075327

Fourriere, L., S. Divoux, M. Roceri, F. Perez, and G. Boncompain. 2016. Microtubule-independent secretion requires functional maturation of Golgi elements. *J. Cell Sci.* 129:3238–3250. https://doi.org/10.1242/jcs.188870

Glick, B.S., and A. Luini. 2011. Models for Golgi traffic: A critical assessment. *Cold Spring Harb Perspect. Biol.* 3:a005215. https://doi.org/10.1101/cshperspect.a005215

Guo, Y., D.W. Sirkis, and R. Schekman. 2014. Protein sorting at the trans-Golgi network. *Annu. Rev. Cell Dev. Biol.* 30:169–206. https://doi.org/10.1146/annurev-cellbio-100913-013012

Hao, X., E.S. Allgeyer, D.R. Lee, J. Antonello, K. Watters, J.A. Gerdes, L.K. Schroeder, F. Bottanelli, J. Zhao, P. Kidd, et al. 2021. Three-dimensional adaptive optical nanoscopy for thick specimen imaging at sub-50-nm resolution. *Nat. Methods.* 18:688–693. https://doi.org/10.1038/s41592-021-01149-9

Hay, J.C., J. Klumperman, V. Oorschot, M. Steegmaier, C.S. Kuo, and R.H. Scheller. 1998. Localization, dynamics, and protein interactions reveal distinct roles for ER and Golgi SNAREs. *J. Cell Biol.* 141:1489–1502. https://doi.org/10.1083/jcb.141.7.1489

Hughes, H., A. Budnik, K. Schmidt, K.J. Palmer, J. Mantell, C. Noakes, A. Johnson, D.A. Carter, P. Verkade, P. Watson, and D.J. Stephens. 2009. Organisation of human ER-exit sites: Requirements for the localisation of Sec16 to transitional ER. *J. Cell Sci.* 122:2924–2934. https://doi.org/10.1242/jcs.044032

Klumperman, J., A. Schweizer, H. Clausen, B.L. Tang, W. Hong, V. Oorschot, and H.P. Hauri. 1998. The recycling pathway of protein ERGIC-53 and dynamics of the ER-Golgi intermediate compartment. *J. Cell Sci.* 111:3411–3425. https://doi.org/10.1242/jcs.111.22.3411

Koreishi, M., T.J. Gniadek, S. Yu, J. Masuda, Y. Honjo, and A. Satoh. 2013. The golgin tether giantin regulates the secretory pathway by controlling stack organization within Golgi apparatus. *PLoS One.* 8:e59821. https://doi.org/10.1371/journal.pone.0059821

Ladinsky, M.S., D.N. Mastronarde, J.R. McIntosh, K.E. Howell, and L.A. Staehelin. 1999. Golgi structure in three dimensions: Functional insights from the normal rat kidney cell. *J. Cell Biol.* 144:1135–1149. https://doi.org/10.1083/jcb.144.6.1135

Lavieu, G., M.H. Dunlop, A. Lerich, H. Zheng, F. Bottanelli, and J.E. Rothman. 2014. The Golgi ribbon structure facilitates anterograde transport of large cargoes. *Mol. Biol. Cell.* 25:3028–3036. https://doi.org/10.1091/mbc.E14-04-0931

Linstedt, A.D., A. Mehta, J. Suhan, H. Reggio, and H.P. Hauri. 1997. Sequence and overexpression of GPP130/GIMPc: Evidence for saturable pH-sensitive targeting of a type II early Golgi membrane protein. *Mol. Biol. Cell.* 8:1073–1087. https://doi.org/10.1091/mbc.8.6.1073

Losev, E., C.A. Reinke, J. Jellen, D.E. Strongin, B.J. Bevis, and B.S. Glick. 2006. Golgi maturation visualized in living yeast. *Nature.* 441:1002–1006. https://doi.org/10.1038/nature04717

Lu, L., G. Tai, M. Wu, H. Song, and W. Hong. 2006. Multilayer interactions determine the Golgi localization of GRIP golgins. *Traffic.* 7:1399–1407. https://doi.org/10.1111/j.1600-0854.2006.00473.x

Marsh, B.J., D.N. Mastronarde, K.F. Buttle, K.E. Howell, and J.R. McIntosh. 2001. Organellar relationships in the Golgi region of the pancreatic beta

cell line, HIT-T15, visualized by high resolution electron tomography. *Proc. Natl. Acad. Sci. USA*. 98:2399–2406. https://doi.org/10.1073/pnas.051631998

Matlin, K.S., and K. Simons. 1983. Reduced temperature prevents transfer of a membrane glycoprotein to the cell surface but does not prevent terminal glycosylation. *Cell*. 34:233–243. https://doi.org/10.1016/0092-8674(83)90154-x

Matsuura-Tokita, K., M. Takeuchi, A. Ichihara, K. Mikuriya, and A. Nakano. 2006. Live imaging of yeast Golgi cisternal maturation. *Nature*. 441: 1007–1010. https://doi.org/10.1038/nature04737

Moelleken, J., J. Malsam, M.J. Betts, A. Movafeghi, I. Reckmann, I. Meissner, A. Hellwig, R.B. Russell, T. Sollner, B. Brugger, and F.T. Wieland. 2007. Differential localization of coatomer complex isoforms within the Golgi apparatus. *Proc. Natl. Acad. Sci. USA*. 104:4425–4430. https://doi.org/10.1073/pnas.0611360104

Mogelsvang, S., B.J. Marsh, M.S. Ladinsky, and K.E. Howell. 2004. Predicting function from structure: 3D structure studies of the mammalian Golgi complex. *Traffic*. 5:338–345. https://doi.org/10.1111/j.1398-9219.2004.00186.x

Orci, L., M. Stamnes, M. Ravazzola, M. Amherdt, A. Perrelet, T.H. Sollner, and J.E. Rothman. 1997. Bidirectional transport by distinct populations of COPI-coated vesicles. *Cell*. 90:335–349. https://doi.org/10.1016/s0092-8674(00)80341-4

Patterson, G.H., K. Hirschberg, R.S. Polishchuk, D. Gerlich, R.D. Phair, and J. Lippincott-Schwartz. 2008. Transport through the Golgi apparatus by rapid partitioning within a two-phase membrane system. *Cell*. 133: 1055–1067. https://doi.org/10.1016/j.cell.2008.04.044

Puertollano, R., N.N. van der Wel, L.E. Greene, E. Eisenberg, P.J. Peters, and J.S. Bonifacino. 2003. Morphology and dynamics of clathrin/GGA1-coated carriers budding from the trans-Golgi network. *Mol. Biol. Cell*. 14: 1545–1557. https://doi.org/10.1091/mbc.02-07-0109

Rogalski, A.A., J.E. Bergmann, and S.J. Singer. 1984. Effect of microtubule assembly status on the intracellular processing and surface expression of an integral protein of the plasma membrane. *J. Cell Biol.* 99:1101–1109. https://doi.org/10.1083/jcb.99.3.1101

Saraste, J., and E. Kuismanen. 1984. Pre- and post-Golgi vacuoles operate in the transport of Semliki Forest virus membrane glycoproteins to the cell surface. *Cell*. 38:535–549. https://doi.org/10.1016/0092-8674(84)90508-7

Scales, S.J., R. Pepperkok, and T.E. Kreis. 1997. Visualization of ER-to-Golgi transport in living cells reveals a sequential mode of action for COPII and COPI. *Cell*. 90:1137–1148. https://doi.org/10.1016/s0092-8674(00)80379-7

Spooner, R.A., P. Watson, D.C. Smith, F. Boal, M. Amessou, L. Johannes, G.J. Clarkson, J.M. Lord, D.J. Stephens, and L.M. Roberts. 2008. The secretion inhibitor Exo2 perturbs trafficking of Shiga toxin between endosomes and the trans-Golgi network. *Biochem. J.* 414:471–484. https://doi.org/10.1042/BJ20080149

Staehelin, L.A., and B.H. Kang. 2008. Nanoscale architecture of endoplasmic reticulum export sites and of Golgi membranes as determined by electron tomography. *Plant Physiol.* 147:1454–1468. https://doi.org/10.1104/pp.108.120618

Steegmaier, M., J. Klumperman, D.L. Foletti, J.S. Yoo, and R.H. Scheller. 1999. Vesicle-associated membrane protein 4 is implicated in trans-Golgi network vesicle trafficking. *Mol. Biol. Cell*. 10:1957–1972. https://doi.org/10.1091/mbc.10.6.1957

Stephens, D.J., N. Lin-Marq, A. Pagano, R. Pepperkok, and J.P. Paccaud. 2000. COPI-coated ER-to-Golgi transport complexes segregate from COPII in close proximity to ER exit sites. *J. Cell Sci.* 113:2177–2185

Sun, X., D. Mahajan, B. Chen, Z. Song, and L. Lu. 2021. A quantitative study of the Golgi retention of glycosyltransferases. *J. Cell Sci.* 134:jcs258564. https://doi.org/10.1242/jcs.258564

Sun, X., H.C. Tie, B. Chen, and L. Lu. 2020. Glycans function as a Golgi export signal to promote the constitutive exocytic trafficking. *J. Biol. Chem.* 295: 14750–14762. https://doi.org/10.1074/jbc.RA120.014476

Tang, B.L., T. Zhang, D.Y. Low, E.T. Wong, H. Horstmann, and W. Hong. 2000. Mammalian homologues of yeast sec31p. An ubiquitously expressed form is localized to endoplasmic reticulum (ER) exit sites and is essential for ER-Golgi transport. *J. Biol. Chem.* 275:13597–13604. https://doi.org/10.1074/jbc.275.18.13597

Tie, H.C., B. Chen, X. Sun, L. Cheng, and L. Lu. 2017. Quantitative localization of a Golgi protein by imaging its center of fluorescence mass. *J. Vis. Exp.* 55996. https://doi.org/10.3791/55996

Tie, H.C., A. Ludwig, S. Sandin, and L. Lu. 2018. The spatial separation of processing and transport functions to the interior and periphery of the Golgi stack. *Elife*. 7:e41301. https://doi.org/10.7554/eLife.41301

Tie, H.C., D. Mahajan, B. Chen, L. Cheng, A.M.J. VanDongen, and L. Lu. 2016. A novel imaging method for quantitative Golgi localization reveals differential intra-Golgi trafficking of secretory cargoes. *Mol. Biol. Cell*. 27:848–861. https://doi.org/10.1091/mbc.E15-09-0664

Tran, T.H.T., Q. Zeng, and W. Hong. 2007. VAMP4 cycles from the cell surface to the trans-Golgi network via sorting and recycling endosomes. *J. Cell Sci.* 120:1028–1041. https://doi.org/10.1242/jcs.03387

Trucco, A., R.S. Polishchuk, O. Martella, A. Di Pentima, A. Fusella, D. Di Giandomenico, E. San Pietro, G.V. Beznoussenko, E.V. Polishchuk, M. Baldassarre, et al. 2004. Secretory traffic triggers the formation of tubular continuities across Golgi sub-compartments. *Nat. Cell Biol.* 6: 1071–1081. https://doi.org/10.1038/ncb1180

Van De Moortele, S., R. Picart, A. Tixier-Vidal, and C. Tougard. 1993. Nocodazole and taxol affect subcellular compartments but not secretory activity of GH3B6 prolactin cells. *Eur. J. Cell Biol.* 60:217–227

von Blume, J., A.M. Alleaume, C. Kienzle, A. Carreras-Sureda, M. Valverde, and V. Malhotra. 2012. Cab45 is required for Ca^{2+}-dependent secretory cargo sorting at the trans-Golgi network. *J. Cell Biol.* 199:1057–1066. https://doi.org/10.1083/jcb.201207180

Weigel, A.V., C.L. Chang, G. Shtengel, C.S. Xu, D.P. Hoffman, M. Freeman, N. Iyer, J. Aaron, S. Khuon, J. Bogovic, et al. 2021. ER-to-Golgi protein delivery through an interwoven, tubular network extending from ER. *Cell*. 184:2412–2429.e16. https://doi.org/10.1016/j.cell.2021.03.035

Zhang, Y., L.K. Schroeder, M.D. Lessard, P. Kidd, J. Chung, Y. Song, L. Benedetti, Y. Li, J. Ries, J.B. Grimm, et al. 2020. Nanoscale subcellular architecture revealed by multicolor three-dimensional salvaged fluorescence imaging. *Nat. Methods*. 17:225–231. https://doi.org/10.1038/s41592-019-0676-4

JCB

Supplemental material

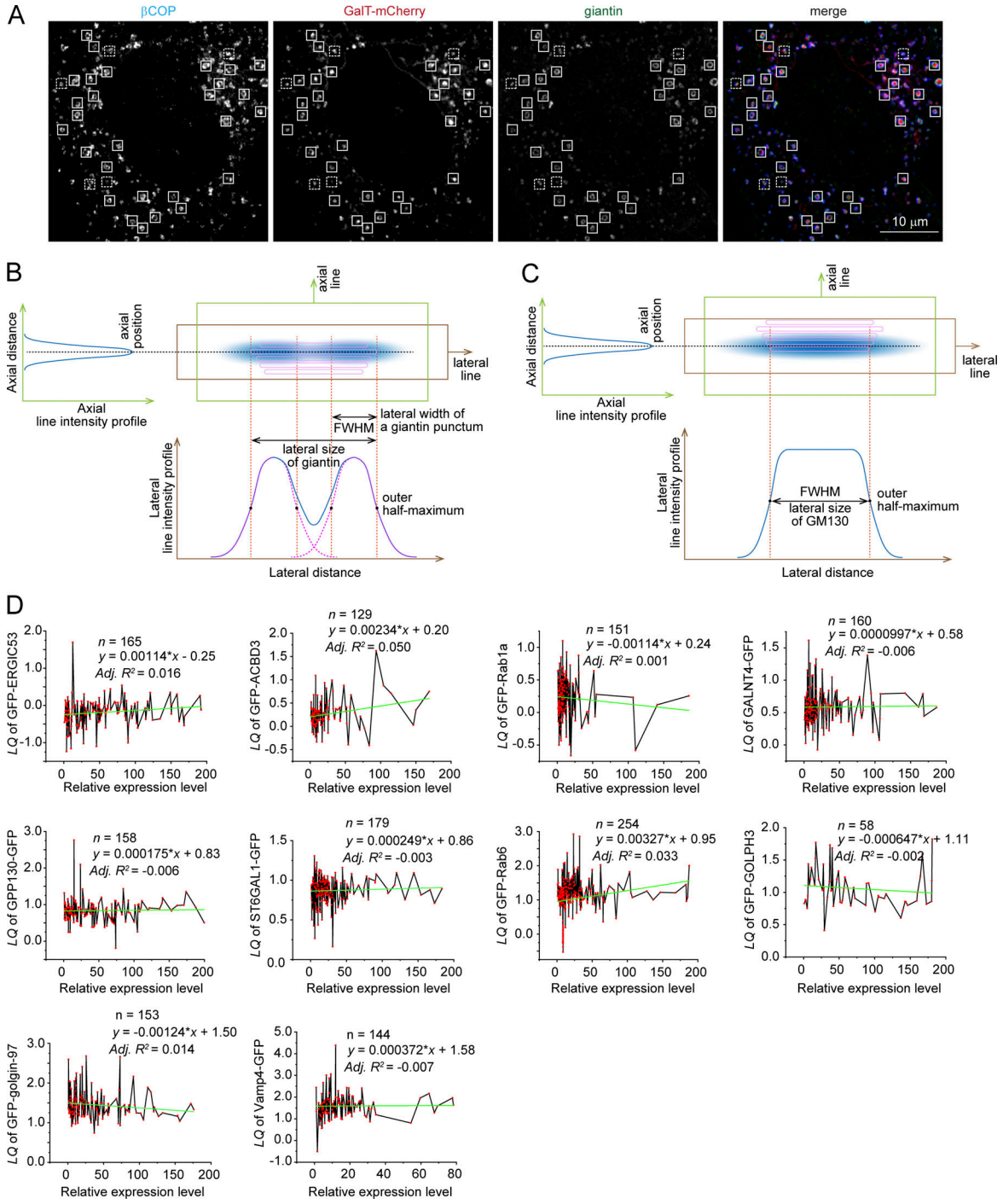

Figure S1. **Giantin distribution among ministacks, morphometric parameters of a side-view ministack, and the effect of overexpression on the *LQ*.** **(A)** HeLa cells expressing GalT-mCherry were nocodazole-treated for 3 h and immunostained for giantin and βCOP. The Airyscan image demonstrates that almost all ministacks are positive for giantin. Box with a solid line, en face view. Box with a dotted line, side-view. Scale bar, 10 μm. **(B and C)** Diagrams illustrating the morphometric parameters of a side-view ministack. **(B)** The rim-localized Golgi protein such as giantin. **(C)** The interior-localized Golgi protein such as GM130. The side-view of the ministack is positioned such that the trans side is up and the Golgi axis is vertical. An imaginary Golgi ministack is schematically overlaid (pink). The axial line intensity profile is acquired along the axial line (green vertical box). The axial position is defined as the fluorescence center or the Gaussian center of the axial line intensity profile. The lateral line intensity profile is acquired along the lateral line (brown horizontal box). The lateral line intensity profile of the rim-localized Golgi protein such as giantin (B) is different from that of the interior-localized one such as GM130 (C). Typically, the former has the two-peak Gaussian distribution, while the latter has the super-Gaussian distribution. The lateral width of a punctum for giantin and the lateral size are schematically illustrated in the diagram. **(D)** Investigating the effect of overexpression on the *LQ*. 10 GFP-tagged Golgi proteins were selected for investigation. For each ministack, the *LQ* was plotted against the corresponding relative expression level of the protein as a red dot. The relative expression level was calculated as the integrated intensity of the protein divided by that of endogenous GM130 in a ministack. It was further normalized such that the lowest value is 1. Black lines were used to connect red dots from low to high relative expression levels. The linear regression fitting line (green) and its formula, adjusted R^2 (adj. R^2), and *n* (the number of ministacks analyzed) are shown.

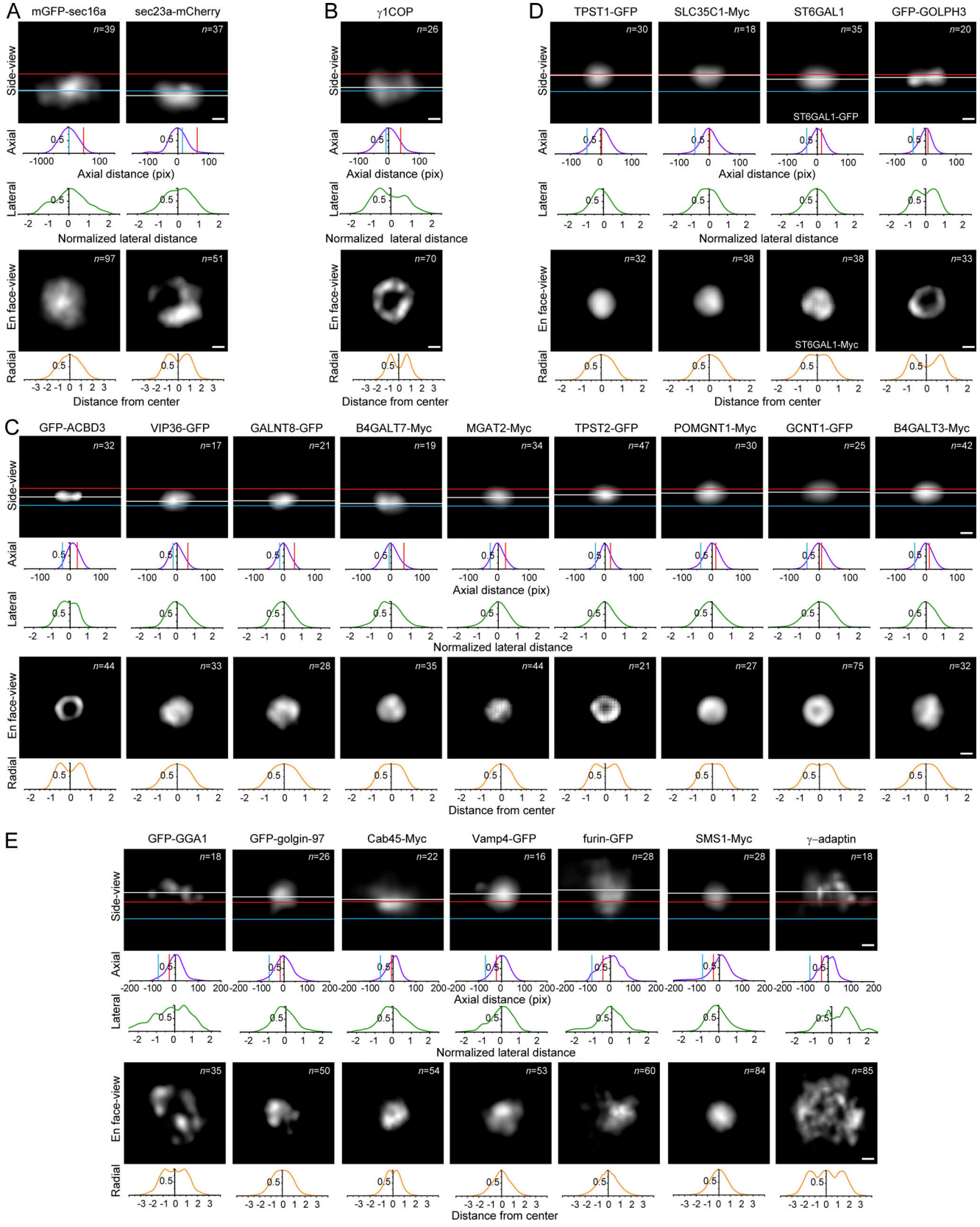

Figure S2. **Images and plots of side-averaged Golgi proteins. (A)** ERES protein: mGFP-sec16a and sec23a-mCherry. **(B)** cis-Golgi protein: γ1COP. **(C)** medial-Golgi proteins: GFP-ACBD3, VIP36-GFP, GALNT8-GFP, B4GALT7-Myc, MGAT2-Myc, TPST2-GFP, POMGNT1-Myc, GCNT1-GFP, and B4GALT3-Myc. **(D)** trans-Golgi proteins: TPST1-GFP, SLC35C1-Myc, ST6GAL1-GFP (or ST6GAL1-Myc), and GFP-GOLPH3. **(E)** TGN proteins: GFP-GGA1, GFP-golgin-97, Cab45-Myc, Vamp4-GFP, furin-GFP, SMS1-Myc, and γ-adaptin. Panels are organized as in Fig. 2, A–D. Proteins are arranged by their *LQ*s. Scale bar, 200 nm.

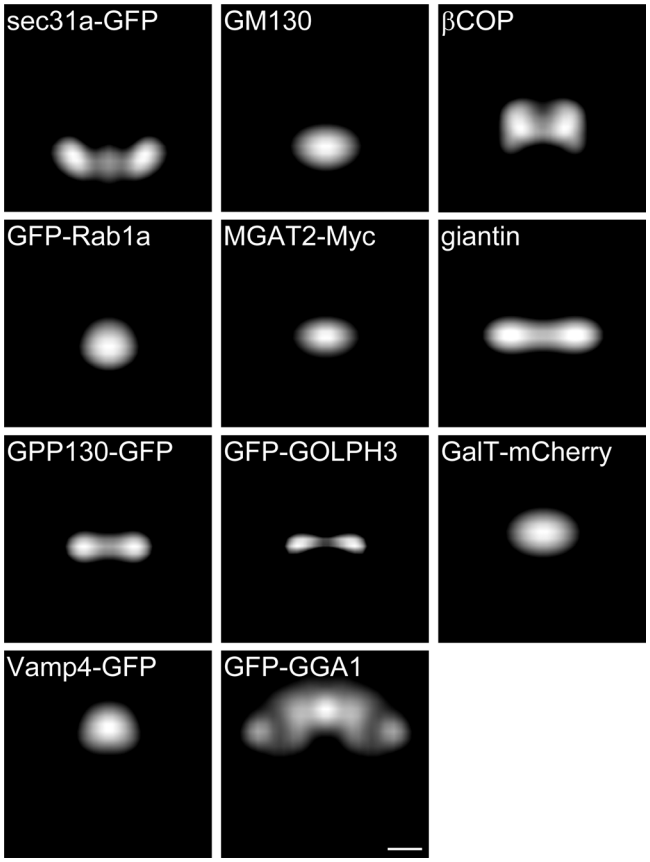

Figure S3. **Images of reflection-averaged Golgi proteins used in Fig. 3 A.** Selected side-averaged Golgi proteins in Figs. 2 and S2 are further subjected to reflection averaging. Scale bar, 200 nm.

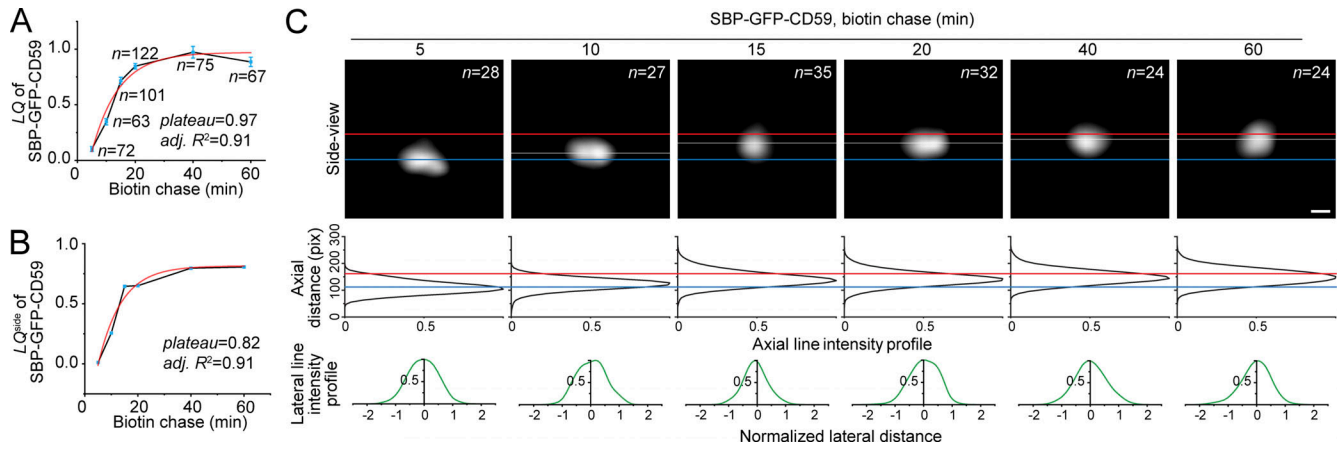

Figure S4. **Imaging the intra-Golgi secretory transport of CD59 by side-averaging. (A–C)** The experiments and the organization of panels are similar to those of Fig. 4, A–C. Scale bar, 200 nm.

Provided online are Table S1, Table S2, Table S3, Data S1, Data S2, and Data S3. Table S1 lists terms and variables defined or used in this study. Table S2 lists comparison between side-average data and corresponding published EM localization results. Table S3 lists the DNA plasmids and construction methods. Data S1 provides the code for the Fiji macro "P1-Rotate_Resize_Normalize." Data S2 provides the code for the Fiji macro "P2-Resize_Add_Line." Data S3 provides the code for the Fiji macro "P3-Refelection_Average."